

Modes and instabilities in magnetized spherical Couette flow

A. FIGUEROA, N. SCHAEFFER,
H.-C. NATAF[†], AND D. SCHMITT

ISTerre, Université de Grenoble 1, CNRS, F-38041 Grenoble, France

(Received ?; revised ?; accepted ?. - To be entered by editorial office)

Several teams have reported peculiar frequency spectra for flows in a spherical shell. To address their origin, we perform numerical simulations of the spherical Couette flow in a dipolar magnetic field, in the configuration of the *DTS* experiment. The frequency spectra computed from time-series of the induced magnetic field display similar bumpy spectra, where each bump corresponds to a given azimuthal wave number m . The bumps show up at moderate Reynolds number ($\simeq 2600$) if the time-series are long enough (> 300 rotations of the inner sphere). We present a new method that permits to retrieve the dominant frequencies for individual wave numbers m , and to extract the non-linear modal structure of the flow. The maps of the energy of the fluctuations and the spatio-temporal evolution of the velocity field suggest that fluctuations originate in the outer boundary layer. Comparisons with the linear stability analysis of this Bödewadt layer confirm this hypothesis. We explore the variation of the magnetic and kinetic energies with the input parameters, and show that a modified Elsasser number controls their evolution. We can thus compare with experimental determinations of these energies and find a good agreement. Because of the dipolar nature of the imposed magnetic field, the energy of magnetic fluctuations is much larger near the inner sphere, but their origin lies in velocity fluctuations that initiate in the outer boundary layer. Our results suggest that the contribution of boundary layer instabilities to turbulence in the Earth's liquid core could have been underestimated.

Key words:

1. Introduction

It is now well established that the magnetic field of most planets and stars is generated by the dynamo mechanism (Larmor 1919; Elsasser 1946). Motions within an electrically conducting medium can amplify infinitesimally small magnetic field fluctuations up to a level where the Lorentz force that results is large enough to stop their amplification. This is possible for large enough values of the magnetic Reynolds number $Rm = UL/\eta$ (where U is a typical flow velocity, L a typical length, and η is the magnetic diffusivity of the medium).

Analytical (Busse 1970) and numerical (Glatzmaier & Roberts 1995) convective dynamo models, in which the flow is driven by the buoyancy force of thermal or compositional origin, have demonstrated the relevance of the dynamo mechanism for generating the Earth's magnetic field. Other forcings, due to precession, tides or impacts are also invoked to explain the fields of some other planets (Le Bars *et al.* 2011).

[†] Email address for correspondence: Henri-Claude.Nataf@ujf-grenoble.fr

In year 2000, two experiments demonstrated dynamo action in the lab (Gailitis *et al.* 2001; Stieglitz & Müller 2001). In both cases, the forcing was mechanical, with a dominant large-scale flow. Efforts to produce dynamo action with a highly turbulent flow are still on the way (Lathrop & Forest 2011; Kaplan *et al.* 2011; Frick *et al.* 2010), while a rich variety of dynamo behaviours have been discovered in the *VKS* experiment (Berhanu *et al.* 2007; Monchaux *et al.* 2007) when ferromagnetic disks stir the fluid.

All these experiments use liquid sodium as a working fluid. The magnetic Prandtl number $Pm = \nu/\eta$ of liquid sodium is less than 10^{-5} (ν is the kinematic viscosity), so that experiments that achieve Rm of order 50 (as required for dynamo action) have kinetic Reynolds number $Re = UL/\nu$ in excess of 10^6 . This contrasts with numerical simulations, which require heavy computations with 1024^3 grid points to reach $Re = 10^4$. Since Reynolds numbers of flows in planetary cores and stars are much larger, we have to rely on theory to bridge the gap. Dynamo turbulence is a crucial issue because dissipation is very much dependent upon the scale and strength of turbulent fluctuations. The question of instabilities and turbulence is also central in the study of accretion disks (Balbus & Hawley 1991). Laboratory experiments can bring some constraints since they exhibit intermediate Reynolds numbers.

In that respect, the observation in several experiments of very peculiar frequency spectra, characterized by a succession of peaks or bumps deserves some attention. Such bumpy spectra have been obtained in both spherical and cylindrical geometries, when rotation or/and magnetic fields are present, two ingredients that also play a major role in natural systems.

Kelley *et al.* (2007) were the first to observe a bumpy spectrum in a rotating spherical Couette experiment. A small axial magnetic field was applied and the induced field was used as a marker of the flow. The authors showed that the frequency and pattern of the modes correspond to a set of inertial modes. Inertial modes are the oscillatory linear response of a fluid to a time-dependent perturbation where the Coriolis force is the restoring force. Several hypotheses have been put forward to explain the excitation of inertial modes in these experiments: overcritical reflection off the inner Stewartson layer (Kelley *et al.* 2010), and turbulence from the tangent cylinder on the inner sphere (Matsui *et al.* 2011).

Bumpy frequency spectra were also reported by Schmitt *et al.* (2008) in the *DTs* magnetized spherical Couette flow experiment (Cardin *et al.* 2002; Nataf *et al.* 2006, 2008; Brito *et al.* 2011). An example is shown in figure 1a. Schmitt *et al.* (2008) could show, by correlating signals measured at several longitudes, that each bump is characterized by a given azimuthal wavenumber m (figure 1b). Schmitt *et al.* (2012) further investigated the properties of the bumps and showed a good correspondence with linear magneto-inertial modes, in which both the Coriolis and the Lorentz forces play a leading role.

Finally, modes of azimuthal wavenumber $m = 1$ were observed in two magnetized Couette flow experiments aimed at detecting the magneto-rotational instability (MRI): in spherical geometry in Maryland (Sisan *et al.* 2004) and in cylindrical geometry in Princeton (Nornberg *et al.* 2010). Gissinger *et al.* (2011) explained these modes as instabilities of the magnetically-modified Stewartson shear layer that forms on the tangent cylinder of the inner sphere or on velocity discontinuities at the top and bottom lids of the cylindrical experiment.

However, two major questions persist concerning bumpy spectra: how and where are the various modes excited? Are these spectra observed because of the large value of the Reynolds number? The answers to these questions determine the extrapolation that can be drawn to natural systems. In this article, we perform numerical simulations to address these two questions, in the geometry of the *DTs* experiment. We present the numerical

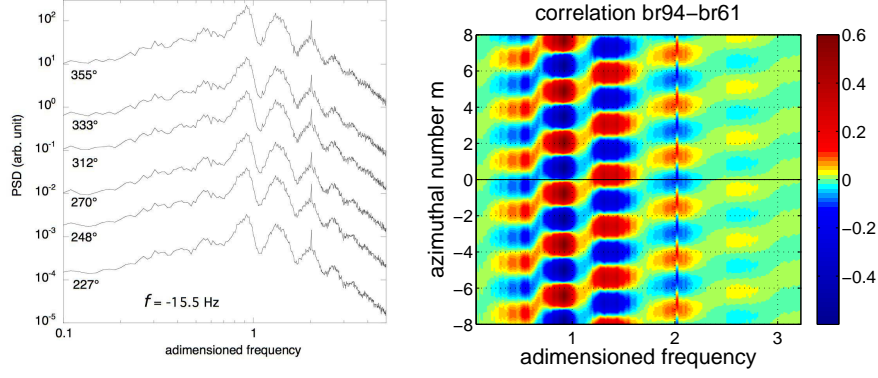


FIGURE 1. Spectral bumps in the *DTS* magnetized spherical Couette flow experiment. a) Frequency spectra of the radial component of the surface magnetic field b_r measured at a latitude of -35° and several longitudes. Frequencies are normalized by the rotation frequency of the inner sphere ($f = -15.5$ Hz). Note the succession of bumps that dominate the spectrum. b) covariance between two b_r time-series recorded at points 128° apart in longitude (same latitude $= -35^\circ$), in a frequency-azimuthal modenumber (m) plot. This plot shows that each spectral bumps in a) corresponds to a well-defined integer m , which increases with frequency (step-wise succession of positive covariance values starting at $m = 0$).

model and the mean flow in section 2. We perform spectral analyses in section 3, and investigate fluctuations and instabilities in section 4. A discussion concludes the article.

2. Numerical model and mean flow

The *DTS* experiment that we wish to model is a spherical Couette flow experiment with an imposed dipolar magnetic field. Liquid sodium is used as a working fluid. It is contained between an inner sphere and a concentric outer shell, from radius $r = b$ to $r = a$ ($b = 74$ mm, $a = 210$ mm). The inner sphere consists of a 15 mm-thick copper shell, which encloses a permanent magnet that produces the imposed magnetic field, whose intensity reaches 175 mT at the equator of the inner sphere. The stainless steel outer shell is 5 mm thick. The inner sphere can rotate around the vertical axis (which is the axis of the dipole) at rotation rates $f = 2\pi\Omega$ up to 30 Hz. Although the outer shell can also rotate independently around the vertical axis in *DTS*, we only consider here the case when the outer sphere is at rest.

All these elements are taken into account in the numerical model, which is sketched in figure 2. In particular, we reproduce the ratio in electric conductivity of the three materials (copper, sodium, stainless steel). In the experiment, the inner sphere is held by 25 mm-diameter stainless steel shafts, which are not included in the numerical model.

2.1. Equations

We solve the Navier-Stokes and magnetic induction equations that govern the evolution of the velocity and magnetic fields of an incompressible fluid in a spherical shell:

$$\frac{\partial \mathbf{u}}{\partial t} + (\mathbf{u} \cdot \nabla) \mathbf{u} = -\frac{1}{\rho} \nabla p + \nu \nabla^2 \mathbf{u} + \frac{1}{\mu_0 \rho} (\nabla \times \mathbf{B}) \times \mathbf{B}, \quad (2.1)$$

$$\frac{\partial \mathbf{B}}{\partial t} = \nabla \times (\mathbf{u} \times \mathbf{B}) - \nabla \times (\eta(r) \nabla \times \mathbf{B}), \quad (2.2)$$

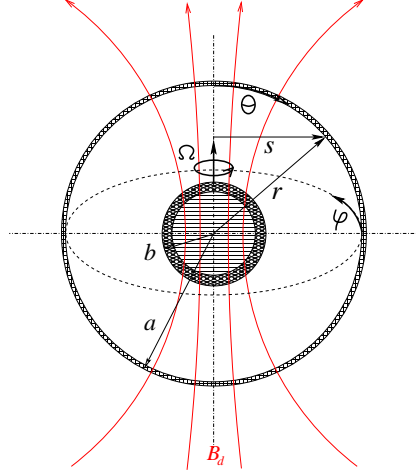


FIGURE 2. Sketch of the *DTS* experiment as modeled in this article. The inner sphere of radius b rotates around the vertical axis at angular velocity Ω . It consists in a copper shell enclosing a permanent magnet, which produces the imposed dipolar magnetic field \mathbf{B}_d . Liquid sodium of electric conductivity σ fills the gap between the inner sphere and the stainless steel outer shell of inner radius a . The spherical coordinate system we use is drawn.

$$\nabla \cdot \mathbf{u} = 0, \quad \nabla \cdot \mathbf{B} = 0, \quad (2.3)$$

where \mathbf{u} and p stand for the velocity and pressure fields respectively. Time is denoted by t , while ρ and ν are the density and kinematic viscosity of the fluid. The magnetic diffusivity $\eta(r)$ is given by $\eta(r) = (\mu_0 \sigma(r))^{-1}$ where $\sigma(r)$ is the electric conductivity of the medium (fluid or solid shells) and μ_0 the magnetic permeability of vacuum. In the fluid, the conductivity $\sigma(r) = \sigma_{Na}$ is constant. The last term of the first equation is the Lorentz force. \mathbf{B} is the magnetic field. It contains the imposed dipolar magnetic field \mathbf{B}_d given by:

$$\mathbf{B}_d = B_0 \frac{a^3}{r^3} (2 \cos \theta \mathbf{e}_r + \sin \theta \mathbf{e}_\theta), \quad (2.4)$$

where θ is the colatitude, \mathbf{e}_r and \mathbf{e}_θ are the unitary vectors in the radial and orthoradial directions. B_0 is the intensity of the field at the equator on the outer surface of the fluid ($r = a$).

2.2. Boundary conditions

We use no-slip boundary conditions for the velocity field on the inner and outer surfaces:

$$\mathbf{u} = \Omega r \sin \theta \mathbf{e}_\varphi \quad \text{for } r \leq b, \quad \mathbf{u} = \mathbf{0} \quad \text{for } r \geq a. \quad (2.5)$$

We model the copper shell that holds the magnet in *DTS* as a conductive shell with electric conductivity $\sigma_{Cu} = 4.2\sigma_{Na}$. The outer stainless steel shell is modelled as a shell of conductivity $\sigma_{SS} = \sigma_{Na}/9$. These values reproduce the experimental conductivity contrasts. The conductivity jumps are implemented by taking a continuous radial conductivity profile with sharp localized variations at both interfaces (3 to 5 densified grid points). The internal magnet and the medium beyond the outer stainless steel shell are modelled as electric insulators. The magnetic field thus matches potential fields at the inner and outer surfaces.

symbol	expression	simulations fixed Ha	simulations fixed Re	DTS $f = [3 - 30]$ Hz	Earth's core
Pm	ν/η	10^{-3}	10^{-3}	7×10^{-6}	10^{-6}
Re	$\Omega ba/\nu$	$[2\,611 - 10\,100]$	2 611	$[0.45 - 4.5] \times 10^6$	10^9
Λ	$\sigma B_0^2/\rho\Omega$	$[3.4 - 0.9] \times 10^{-2}$	$[0.21 - 13.1] \times 10^{-2}$	$[3 - 0.3] \times 10^{-2}$	10
Ha	$aB_0/\sqrt{\rho\mu_0\nu\eta}$	16	$[4 - 31]$	200	10^8

TABLE 1. Typical values of the dimensionless numbers in the numerical simulations, in the DTS experiment (computed for $f = \Omega/2\pi = 3 - 30$ Hz) and in the Earth's core.

2.3. Numerical scheme

Our three-dimensional spherical code (XSHELLS) uses second-order finite differences in radius and pseudo-spectral spherical harmonic expansion, for which it relies on the very efficient spherical harmonic transform of the **SHTns** library (Schaeffer 2012). It performs the time-stepping of the momentum equation in the fluid spherical shell, and the time-stepping of the induction equation both in the conducting walls and in the fluid. It uses a semi-implicit Crank-Nicholson scheme for the diffusive terms, while the non-linear terms are handled by an Adams-Bashforth scheme (second order in time). The simulations that we present typically have 600 radial grid points (with a significant concentration near the interfaces) while the spherical harmonic expansion is carried up to degree 120 and order 40.

2.4. Dimensionless parameters

We define in table 1 the dimensionless numbers that govern the solutions in our problem. We pick the outer radius a as a length scale, and B_0 , the intensity of the magnetic field at the equator of the outer surface, as a magnetic field scale. Note that, due to the dipolar nature of the imposed magnetic field, its intensity is 23 times larger at the equator of the inner sphere. The angular velocity of the inner sphere yields the inverse of the time scale. We choose $U = \Omega b$, the tangential velocity at the equator of the inner sphere, as typical velocity.

The magnetic Prandtl number Pm compares the diffusion of momentum to that of the magnetic field. It is small in both the simulations and the experiment. The Reynolds number Re is of course essential, as it determines the level of fluctuations. It is not feasible to run numerical simulations with Reynolds numbers as large as in the DTS experiment.

However, one of the main findings of Brito *et al.* (2011) is that, because of the imposed dipolar magnetic field, the time-averaged flow is mainly governed by the balance between the Lorentz and the Coriolis forces, where the latter is due to the global rotation of the fluid, which is very efficiently entrained by the inner sphere, even when the outer sphere is at rest. That balance is measured by the Elsasser number Λ . Brito *et al.* (2011) showed that one can recover the proper balance at achievable values of Re by reducing the influence of the magnetic field, keeping the effective Elsasser number Λ as in the experiment.

Nevertheless, Cardin *et al.* (2002) introduced another number λ (named the Lehnert number by Jault (2008)), which provides a better measure of this balance for fast time-dependent phenomena. The Lehnert number λ compares the periods of Alfvén waves to that of inertial waves. It is given by:

$$\lambda = \frac{B_0}{\Omega b \sqrt{\rho\mu_0}}. \quad (2.6)$$

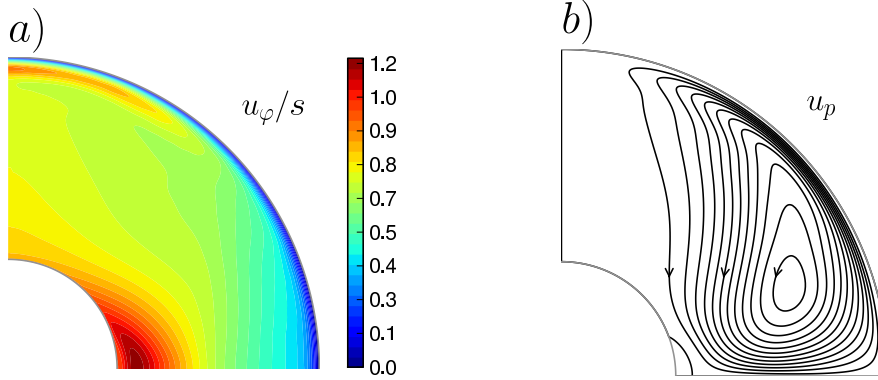


FIGURE 3. Time-averaged meridional slice of the velocity field. a) Angular velocity isovalues. Note the zone of super-rotation near the inner sphere. b) Meridional streamlines. The maximum meridional velocity is 0.4. $Pm = 10^{-3}$, $Re = 2611$, $\Lambda = 3.4 \times 10^{-2}$.

In the Earth's core, this number is of order 10^{-4} and inertial waves dominate. They force the flow to be quasi-geostrophic on short time-scales (Jault 2008). However, magnetic diffusion severely limits the propagation of Alfvén waves in the *DTS* experiment. This is measured by the Lundquist number, which is the ratio of the magnetic diffusion time to the typical transit time of an Alfvén wave across the sphere, here given by:

$$Lu = \frac{aB_0}{\eta\sqrt{\rho\mu_0}}, \quad (2.7)$$

which is taken as $Lu = 0.5$ in the numerical simulations, in agreement with the experimental value.

We therefore follow the same strategy as Brito *et al.* (2011), and try to keep the Elsasser number of the numerical simulations similar to its experimental value. Our reference case thus has: $Pm = 10^{-3}$, $Re = 2611$ and $\Lambda = 3.4 \times 10^{-2}$. The Hartmann number is $Ha = 16$, quite smaller than its experimental counterpart ($Ha = 200$). It follows that $\lambda = 6.8 \times 10^{-2}$ and $Rm = RePm = 2.6$ for the reference case. Most results shown in this article relate to our reference case, but we also present some results computed for other Reynolds and Hartmann numbers, as indicated in table 1.

2.5. Mean flow

The time-averaged properties of the magnetized spherical Couette flow have been investigated in detail by Brito *et al.* (2011), and we simply recall here a few key observations. We plot in figure 3 the time-averaged velocity field in a meridional plane, for our reference simulation ($Pm = 10^{-3}$, $Re = 2611$ and $\Lambda = 3.4 \times 10^{-2}$). Two distinct regions show up in the map of mean angular velocity (figure 3a): an outer geostrophic region, where the angular velocity only varies with the cylindrical radius s ; an inner region that obeys Ferraro law (Ferraro 1937) around the equator: the angular velocity is constant along field lines of the imposed dipolar magnetic field. Note the presence of a thin boundary layer at the outer surface. The poloidal streamlines (figure 3b) display a circulation from the equator towards the poles beneath the outer surface, where the polewards velocity reaches $0.4\Omega b$.

To check our numerical set-up, we compare the time-averaged velocity field of our simulation with that obtained by Brito *et al.* (2011) using an independent axisymmet-

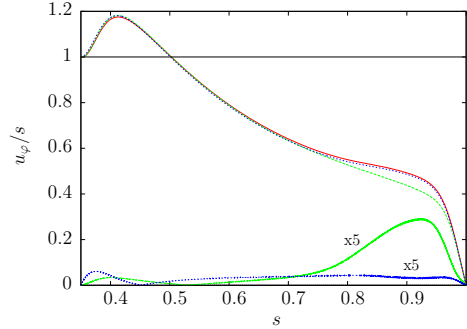


FIGURE 4. Radial profiles of time-averaged angular velocity in the equatorial plane for different simulations with the same parameters ($Pm = 10^{-3}$, $Re = 2611$ and $\Lambda = 3.4 \times 10^{-2}$). Dotted line: axisymmetric equatorially-symmetric solution of Brito *et al.* (2011); solid line: axisymmetric solution computed with our XSHELLS code; dashed line: 3D solution from XSHELLS. The curves at the bottom give the unsigned difference between the 3D solution and the axisymmetric one, and between the two axisymmetric solutions, scaled up by a factor 5.

ric equatorially-symmetric code. The parameters and boundary conditions are identical, except that the magnetic boundary condition at $r = a$ is treated in the thin-shell approximation in Brito *et al.* (2011).

Figure 4 compares the radial profile of the angular velocity in the equatorial plane computed by Brito *et al.* (2011) to our axisymmetric solution, averaged over 50 rotation times, and to our 3D spherical solution, averaged over 100 rotation times. The two axisymmetric solutions agree very well, while the 3D solution exhibits a slightly lower angular velocity near the outer surface. Note that the angular velocity of the fluid reaches values as high as 20% larger than that of the inner sphere. This phenomenon of *super-rotation* was first predicted by Dormy *et al.* (1998) in a linear study of magnetized spherical Couette flow. The excess of 20% is in good agreement with the super-rotation measured in the *DTS* experiment for $f = 3$ Hz ($Re = 4.5 \times 10^5$) (Brito *et al.* 2011).

3. Spectra and modes

3.1. Frequency spectra

In order to compare the numerical results to the experimental measurements of the fluctuations, we perform a simulation over a long time-window (600 rotation periods) and record the magnetic field induced at the surface at selected latitudes. We then compute the power spectra of these records as a function of frequency. Typical spectra are shown in figure 5a. A sequence of bumps is clearly visible for both the radial and the azimuthal components of the magnetic field. The spectra do not display power-law behaviour.

We note that long time series (longer than 300 rotation periods) are needed for the spectral bumps to show up clearly. Schmitt *et al.* (2008) construct the experimental spectra from 100 s time-windows, corresponding to more than 500 rotation periods.

3.2. Azimuthal mode number

Pursuing further the comparison with the experimental results, we examine whether the various spectral bumps correspond to specific azimuthal mode numbers. As in Schmitt *et al.* (2008), we correlate the signals computed at the same latitude (41°) but 72° apart in longitude. The signals are first narrow-band filtered, and we plot in figure 5b the amplitude of the covariance (colour scale) as a function of the peak frequency of the filter, for

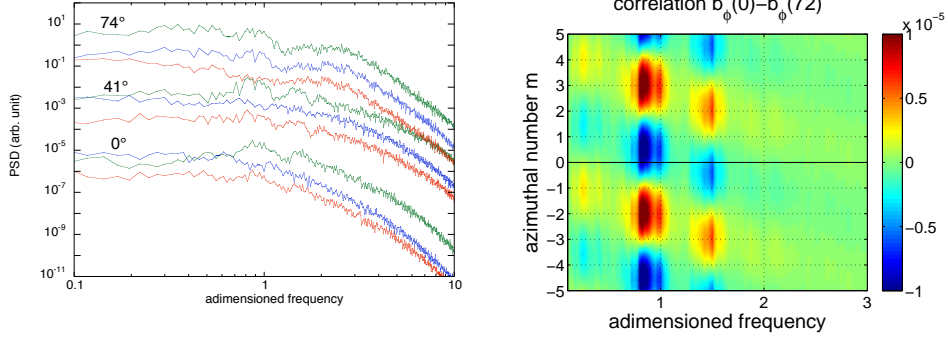


FIGURE 5. Spectral bumps in our reference numerical simulation ($Pm = 10^{-3}$, $Re = 2611$ and $\Lambda = 3.4 \times 10^{-2}$). a) Frequency spectra of the three components of the magnetic field (b_r , b_θ , b_φ in this order going up) recorded at three different latitudes (0° , 41° and 74° as indicated). The spectra are shifted for clarity. Note the spectral bumps for b_φ and b_r and compare with figure 1. b) m versus frequency plot for the same run, obtained from the covariance of two b_φ time-series recorded at points 72° apart in longitude (same latitude = 41°). The red patches for negative m indicate that the successive spectral bumps have a well-defined mode number m , whose absolute value increases with frequency.

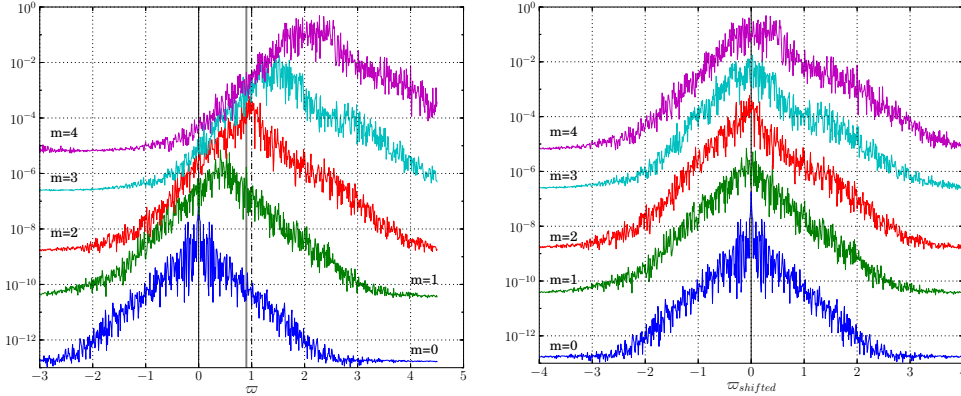


FIGURE 6. Partial energy frequency spectra $\mathcal{E}_m(\varpi)$ of the equatorially-symmetric magnetic field at $r < 0.55$. Frequencies are normalized by f , the rotation frequency of the inner sphere (vertical dashed line). a) Raw spectra for azimuthal mode numbers $m = 0$ to 4 (shifted vertically for clarity). The vertical solid line indicates the frequency ϖ^* at which we retrieve the $m = 2$ mode structure in figure 8. b) Same as a) except that frequencies are shifted according to $\varpi_{\text{shifted}} = \varpi - m f_{\text{fluid}}$ (see text).

time-delays between the two, converted into azimuthal mode number m (y-axis). As in the experiments (see figure 1b), we find that each spectral bump corresponds to a single dominant (here negative by convention) azimuthal mode number m . The successive bumps have increasing azimuthal m (1, 2 and 3).

3.3. Full Fourier transform

In the numerical simulations, we can construct frequency spectra for each m . When the stationary regime is reached, we record 900 snapshots of the full fields, regularly spaced in time during 100 rotation periods: $\mathbf{F}(r, \theta, \varphi, t)$, where \mathbf{F} can be either \mathbf{u} or \mathbf{B} . A two dimensional Fourier transform in the azimuthal and temporal directions φ and t gives us

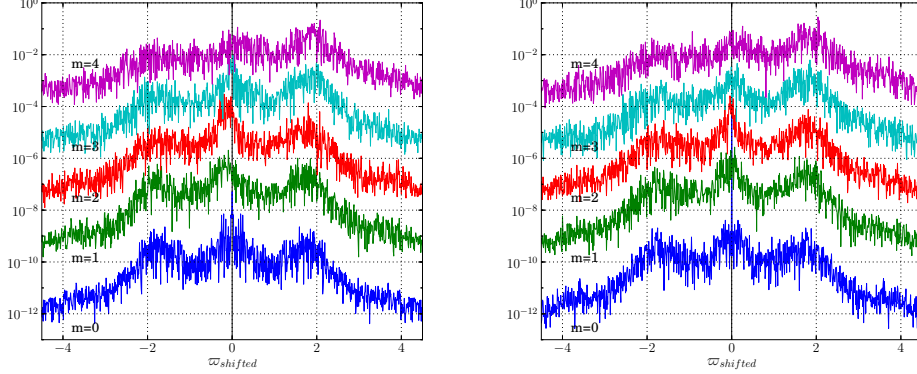


FIGURE 7. Partial energy frequency spectra $\mathcal{E}_m(\varpi)$ of the magnetic field at the outer surface ($1 < r < 1.024$, $0.35 < \sin \theta < 0.6$) for different m . a) Equatorially symmetric part. b) Equatorially-antisymmetric part. Frequencies are normalized by f , the rotation frequency of the inner sphere, and are shifted according to equation 3.3. $Pm = 10^{-3}$, $Re = 2611$ and $\Lambda = 3.4 \times 10^{-2}$.

a collection of complex vectors \mathbf{F}_m^ϖ representing the field for azimuthal number m and discrete frequency ϖ , such that

$$\mathbf{F}(r, \theta, \varphi, t) = \sum_m \sum_{\varpi} \mathbf{F}_m^\varpi(r, \theta) e^{i(m\varphi + \varpi t)}. \quad (3.1)$$

Note that the sign of the frequency has thus a precise meaning: positive (negative) frequencies correspond to prograde (retrograde) waves or modes.

This allows us to compute partial energy spectra

$$\mathcal{E}_m(\varpi) = \int_{r_0}^{r_1} \int_{\theta_0}^{\theta_1} \|\mathbf{F}_m^\varpi(r, \theta)\|^2 r \sin \theta d\theta dr. \quad (3.2)$$

Magnetic partial energy spectra $\mathcal{E}_m(\varpi)$ for the inner region ($0.35 < r < 0.55$, $0 < \theta < \pi$) are shown in figure 6a for $m = 0$ to 4. They are dominated by a single peak, which moves towards positive (prograde) frequencies as m increases. This can be interpreted as the advection of stationary or low-frequency structures by a prograde fluid velocity. We therefore shift the frequency of the spectra in figure 6b, according to:

$$\varpi_{shifted} = \varpi - mf_{fluid} \quad (3.3)$$

A good alignment of the spectral peak is obtained for $f_{fluid} \simeq 0.5$, which is compatible with the bulk fluid velocity in the outer region beneath the boundary layer (see figure 3a). This shift explains the linear evolution of the frequencies of the spectral bumps with m observed both in the *DTS* experiment (figure 1b) and in the simulation (figure 5b).

We now turn to the partial energy spectra of the magnetic field at high latitude ($0.35 < \sin \theta < 0.6$), at the surface of the sphere ($1 < r < 1.024$), displayed in figure 7a and 7b for the equatorially symmetric and anti-symmetric parts, respectively. The frequencies are again shifted according to equation 3.3. This time, three peaks dominate the $m = 0$ spectra. The spectrum is symmetric with respect to $\varpi = 0$ since there cannot be prograde or retrograde propagation for $m = 0$: only latitudinal propagation or time-oscillations are permitted. The lateral peaks yield a frequency $\varpi^\dagger \simeq 1.8$. As m increases, the lateral peak becomes dominant in the prograde direction, while it vanishes in the retrograde direction. We note that the peaks are well aligned in these shifted representation, meaning that

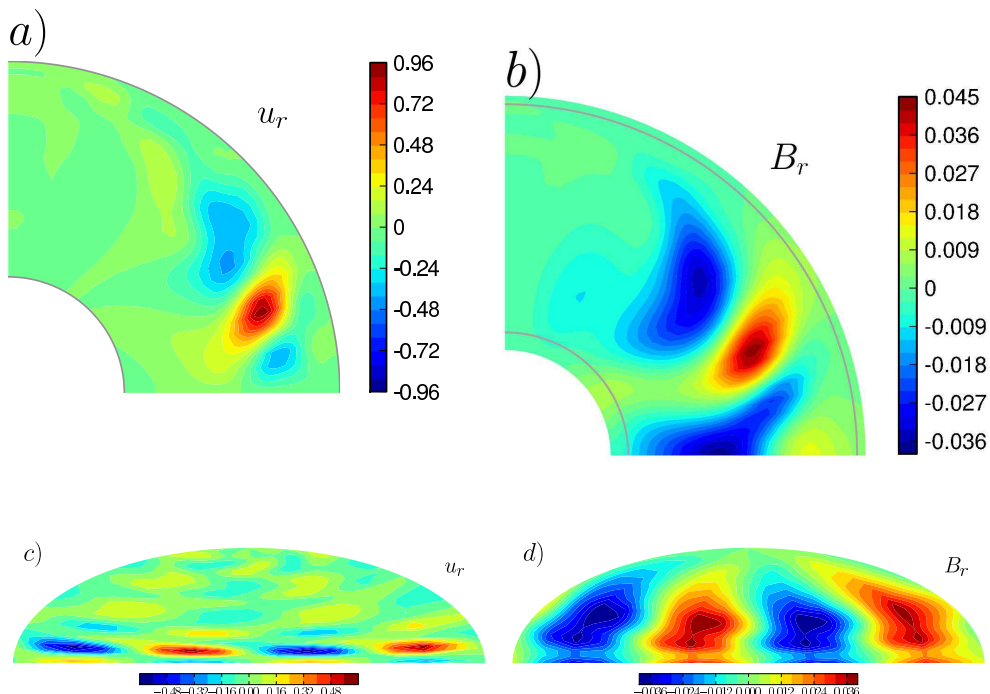


FIGURE 8. $m = 2$ mode structure given by the full Fourier transform method, for frequency $\varpi^* = 0.9$, which corresponds to the $m = 2$ peak in figure 6a. $Pm = 10^{-3}$, $Re = 2611$ and $\Lambda = 3.4 \times 10^{-2}$. Energy densities are normalized by E_K^0 . a) and b) isovalues in the $\varphi = 0^\circ$ meridional plane of the radial velocity and radial magnetic field, respectively. c) and d) mapview of the isovalues at $r = 0.95$ of the radial velocity and radial magnetic field, respectively.

these secondary fluctuations are also advected at roughly the same angular velocity as the central peak.

Note that these secondary peaks do not show up in the regular frequency spectra or m -plots of point-measurements (figure 5). This illustrates the interest and potential of the full Fourier transform method that we developed.

3.4. Mode structure

Picking the frequency that yields the maximum spectral energy density for a given m , we derive the structure of the corresponding mode. One example for $m = 2$ is shown in figure 8, where we plot, for both u_r and B_r , the structure of the mode in a meridional plane and in map view at $r = 0.95$. We selected a mode for which B_r is symmetric with respect to the equator (and thus u_r is anti-symmetric).

The meridional map for u_r reveals structures in the outer region, while B_r shows similar patterns that extend deeper down to the inner sphere. The map view near the outer boundary shows a rather smooth B_r structure, similar to those retrieved in the *DTS* experiment, and well-accounted for in the linear modal approach of Schmitt *et al.* (2012).

4. Fluctuations and instabilities

Having shown that our numerical simulations recover the essential features of the modes and spectra of the *DTS* experiment, even though their Reynolds number is much

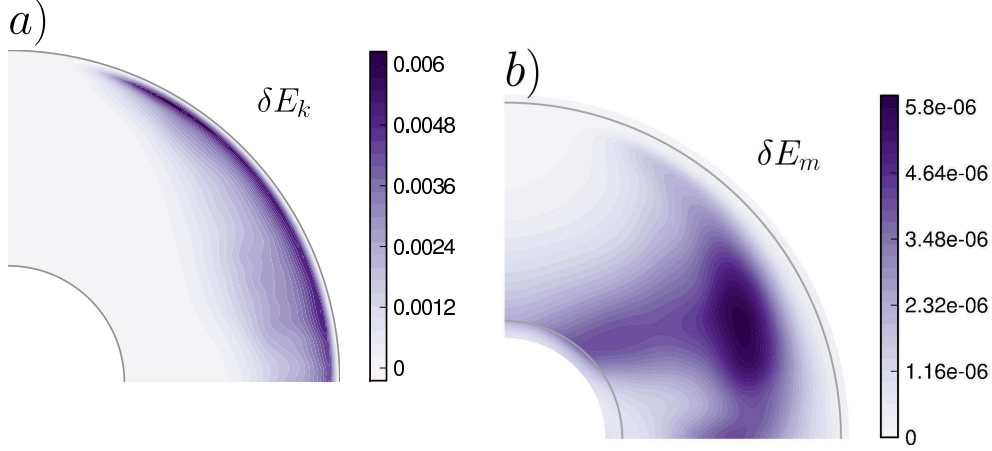


FIGURE 9. Time-and-azimuth-averaged meridional map of the energy of the fluctuations. a) Kinetic energy. b) Magnetic energy. $Pm = 10^{-3}$, $Re = 2611$ and $\Lambda = 3.4 \times 10^{-2}$. The energies are normalized by $E_K^0 = \frac{1}{2}\rho(2\pi f)^2 b^2$.

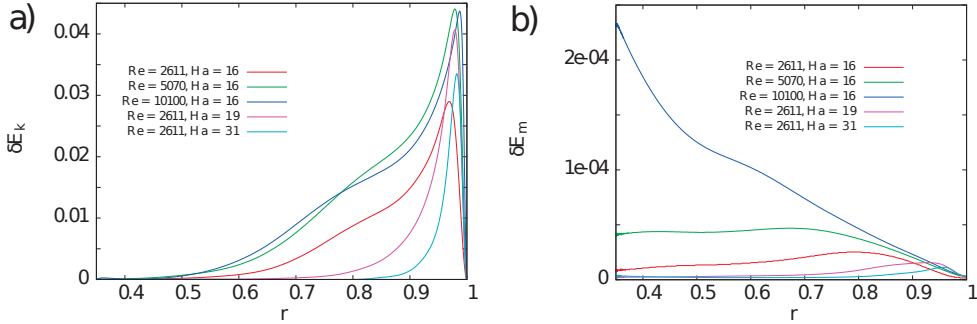


FIGURE 10. Time-angles-averaged energy of the fluctuations as a function of radius r . a) Kinetic energy. b) Magnetic energy. The energies are normalized by E_K^0 . The plots compare the fluctuations obtained for three simulations with the same Hartmann number ($Ha = 16$) and increasing Reynolds numbers ($Re = 2611, 5070$ and 10100), and three simulations with the same Reynolds number ($Re = 2611$) and increasing Hartmann numbers ($Ha = 16, 19$ and 31). Other dimensionless numbers as in Table 1. Note that the magnetic energy is smaller than the kinetic energy by three orders of magnitude, but increases strongly toward the inner sphere for the simulation with the highest Reynolds number.

smaller, we now examine where and how the modes are excited. The first guide we use is the location of the largest fluctuations.

4.1. Energy fluctuations

We compute the kinetic energy density as $\delta E_K = \frac{1}{2}\rho\langle(u - \langle u \rangle)^2\rangle$ and the magnetic energy density as $\delta E_M = \frac{1}{2\mu_0}\langle(b - \langle b \rangle)^2\rangle$, where $\langle \rangle$ denotes time-averaging. We normalize both by a reference kinetic energy density $E_K^0 = \frac{1}{2}\rho\Omega^2 b^2$, and we integrate over azimuth.

Figure 9 displays the resulting kinetic and magnetic energy densities of the fluctuations in a meridional plane for our reference simulation. We observe that the kinetic energy is maximum in the outer boundary layer, while the (much weaker) magnetic energy extends all the way to the inner sphere.

Figure 10 shows the radial profiles obtained after integration over the colatitude θ . It

illustrates the effect of varying the Reynolds and the Hartmann numbers of the simulations. The fluctuations remain strongest in the outer boundary layer, but extend deeper inside the fluid with increasing Reynolds number. For the highest Reynolds number ($Re = 10\,100$), this causes the magnetic energy to strongly increase with depth, as the fluctuations interact with the larger imposed magnetic field near the inner sphere.

4.2. Origin of the fluctuations

The energy maps (figure 9) as well as movies of the simulations (see online supplementary material) strongly suggest that fluctuations are initiated in the outer boundary layer. There is a large azimuthal velocity drop across the outer boundary layer, from the vigorously entrained fluid in the core flow to the outer container at rest. The boundary layer is of the Bödewadt type (Bödewadt 1940), which is known to be particularly unstable (Lingwood 1997).

The instability of a fluid rotating at constant angular velocity above a flat disk at rest (the original Bödewadt situation) has been studied by several groups (e.g., Savas 1987; Lingwood 1997; Lopez *et al.* 2009; Gauthier *et al.* 1999; Schouveiler *et al.* 2001). These studies indicate that the laminar Bödewadt boundary layer becomes unstable when its local Reynolds number exceeds about 22. The local Reynolds number is defined as $Re_l = ul/\nu$, where l is the thickness of the laminar boundary layer: $l = \sqrt{\nu/\Omega}$. We can relate it to our global Reynolds number Re by:

$$Re_l = \omega s \sqrt{\frac{a}{b}} \sqrt{Re}, \quad (4.1)$$

where the angular velocity ω just outside the boundary layer is adimensioned by Ω and the cylindrical radius s by a , as before. Picking $\omega \simeq 0.5$ at the equator of the sphere ($s \simeq 1$) from figure 4, we get $Re_l \simeq 26$ for our reference case with $Re = 2\,611$.

In the disk geometry, two types of instabilities are observed: axisymmetric rolls that propagate inwards (following the centripetal circulation of the boundary layer), and spiral rolls. We observe a very similar behaviour in the early stage of our simulation, when the inner sphere is spun from rest. After 10 turns, axisymmetric downwelling sheets form at the equator and migrate polewards (see online supplementary material). This shows up in the spatio-temporal representations of the instabilities at $r = 0.95$, just beneath the outer boundary layer.

Figure 11a gives the axisymmetric part of u_θ as a function of time (x -axis) and latitude (y -axis). The polewards migrating rings yield a butterfly pattern, which also reveals that the equatorial downwelling instability creates a meridional circulation of opposite sign around the equator. At time $t \simeq 24$ turns, the axisymmetry is broken by an $m = 3$ undulation, which rapidly disrupts the pattern of the fluctuations. Note however that axisymmetric bursts persist throughout, with amplitudes comparable to the initial ones. They propagate mostly polewards, but some occasionally cross the equator.

The $m = 3$ undulation is best observed in the spatio-temporal plot of figure 11b, which displays the non-axisymmetric fluctuations of the azimuthal velocity at a latitude of 10° , as a function of time and longitude (y -axis). A critical azimuthal wavenumber of 3 is compatible with the prediction of Lingwood (1997) for the absolute instability of the Bödewadt boundary layer. She finds indeed that $m_c = \beta_c Re_{l_c} = -0.1174 \times 21.6 \simeq -2.5$. It is very different from the $m_c \simeq 32$ observed in the flat disk geometry (Lopez *et al.* 2009; Schouveiler *et al.* 2001), but reminiscent of the undulations observed by Noir *et al.* (2009) in the experimental study of librations in a sphere. We guess that the condition of parallel flow assumed by Lingwood (1997) is better fit at the equator of a sphere than on the flat disk.

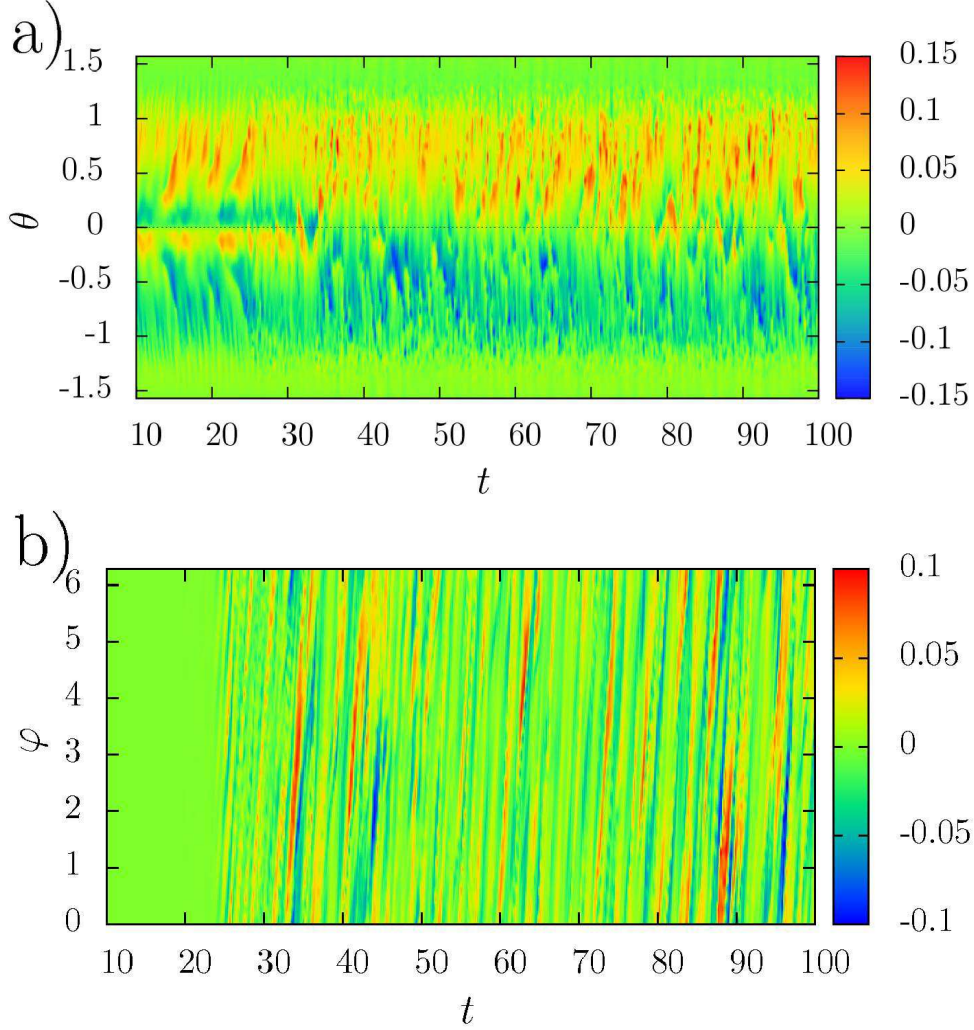


FIGURE 11. Spatio-temporal representation of the velocity fluctuations in the simulation at radius $r = 0.95$. $Pm = 10^{-3}$, $Re = 2611$ and $\Lambda = 3.4 \times 10^{-2}$. a) V_θ isovalues of the axisymmetric flow ($m = 0$) in a latitude-time plot. b) V_ϕ isovalues at 10° latitude in an azimuth-time plot ($m = 0$ term removed). Velocities are normalized by the reference velocity Ωb . Time is given in rotation periods.

In any case, this initial $m = 3$ undulation is rapidly replaced by chaotic fluctuations with dominant $m = 1$ and $m = 2$ contributions, which travel in the prograde direction with approximately the same velocity.

The time-variation of the instabilities at the threshold is given by $\omega_c \simeq -0.218 \times 21.6 \times 0.5 \simeq -2.3$, according to Lingwood's analysis, when we assume again that the local angular velocity drop across the Bödewadt boundary layer is about 0.5 (frequencies and angular velocities are adimensionalized by those of the inner sphere). This value is somewhat larger than the frequency $\varpi^\dagger \simeq 1.8$ of the secondary peak discussed in section 3.3, and displayed in figure 7, which appears to be compatible with the frequency of the instabilities observed at high latitude in the spatio-temporal plot of figure 11a.

Moresco & Alboussière (2004) have investigated the effect of an imposed wall-normal

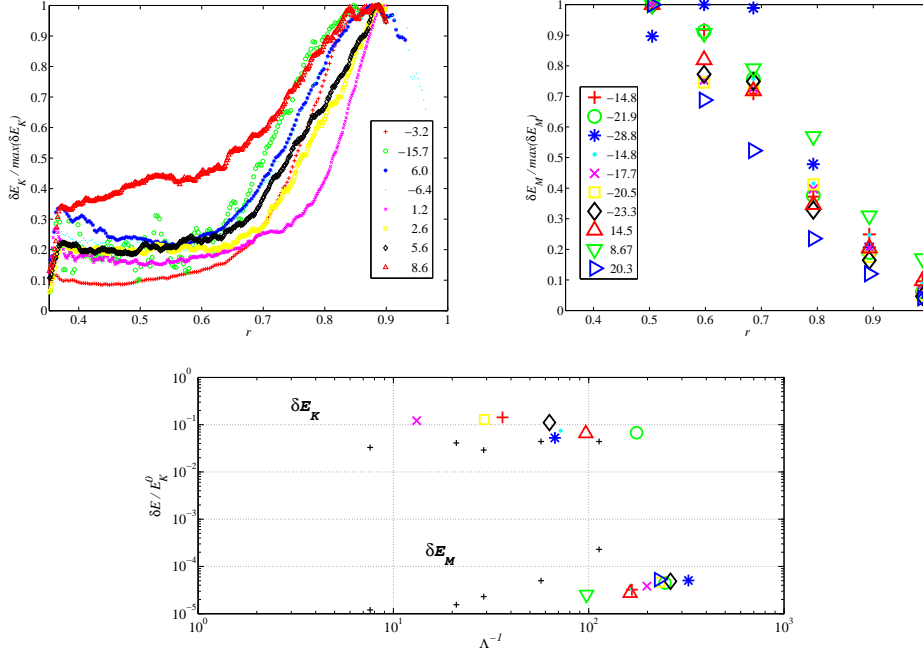


FIGURE 12. Energy of the fluctuations in the *DTS* experiment. a) Radial profiles of the kinetic energy of the fluctuations deduced from ultrasonic Doppler radial velocity measurements at latitude -20° . b) Radial profiles of the magnetic energy of the fluctuations deduced from b_ϕ measurements in a sleeve at latitude 40° . All profiles are normalized by their maximum value, and correspond to different rotation rates f of the inner sphere, given in Hz in the legends. c) Evolution of the kinetic and magnetic energies (normalized by $E_K^0 = \frac{1}{2}\rho\Omega^2 b^2$) as a function of the inverse of the Elsasser number. The black crosses are from the numerical simulations. The colored symbols are deduced from the maximum value of the profiles given in a) and b), using the same markers.

magnetic field on the stability of the Bödewadt boundary layer. The magnetic field smoothes out the inflection points of the laminar profile, thereby increasing the critical Reynolds number. The control parameter is the local Elsasser number $\Lambda_l = \sigma B_{r_l}^2 / \rho \Omega_l$. It can be related to our global Elsasser number Λ by:

$$\Lambda_l = \frac{B_r^2}{\omega} \Lambda, \quad (4.2)$$

where the adimensional angular velocity ω can again be read from figure 4, and the adimensional radial magnetic field is of order one (at a latitude of about 30°). We thus get $\Lambda_l \simeq 0.07$. Interpolating the results of Moresco & Alboussière (2004), this could increase the threshold of instabilities to $Re_{l_c} \simeq 25$, suggesting that our simulations are just above the instability threshold. Note, however, that we observe both axisymmetric and non-axisymmetric instabilities, while the latter are supposed to appear at slightly higher Reynolds numbers.

4.3. Comparison with experimental results

We cannot measure the total kinetic and magnetic energies of the fluctuations in the *DTS* experiment. However, we can get a quantitative assessment of the energy of the fluctuations as a function of radius, at given latitudes. The kinetic energy is obtained from the fluctuations of the radial velocity measured by ultrasound Doppler velocimetry

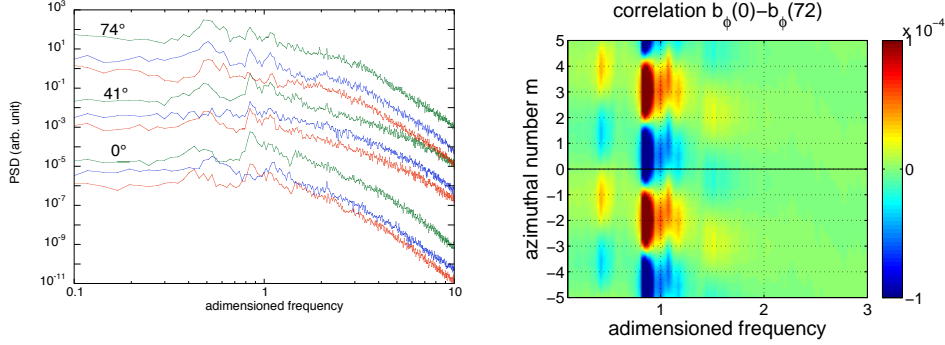


FIGURE 13. Same as figure 5 but for a simulation where the Lorentz force is nulled out for $m \neq 0$. Sharp spectral peaks are observed on all three components of the magnetic field. Neighbouring frequencies can have different azimuthal modenumber m .

along a radial shot at a latitude of -20° . The magnetic energy is derived from the fluctuations of the azimuthal component of the magnetic field measured at a latitude of 40° and at 6 different radii, using Hall probes inserted in a sleeve, after removing a contribution at the rotation frequency f and harmonics, which is due to small heterogeneities of the imposed magnetic field. As for the simulations, we integrate over azimuth by multiplying the measured *rms* by $2\pi r \sin \theta$ and convert to energy. In order to relate to the numerical results, we assume that fluctuations are isotropic. Additional measurements of the magnetic energy from radial and orthoradial probes partly support this hypothesis. Nevertheless, the comparison remains approximative.

The kinetic energy profiles (figure 12a) confirm that fluctuations are strongest near the outer surface. The maximum is deeper than in the numerical simulations (compare with figure 10a, a consequence of the much higher Reynolds number. Note however that the thin viscous boundary layer cannot be resolved from the Doppler velocity profiles.

The magnetic energy profiles (figure 12b) clearly show that fluctuations are strongest near the inner sphere. Figure 10b shows that only the simulation with the highest Reynolds number displays this behaviour.

Figure 12c compares the kinetic and magnetic energies of the fluctuations obtained from both the simulations (black crosses) and the experiments (colored symbols). Since we don't have the full latitudinal dependence in the experiments, we simply take the maximum of each profile as an estimate of the overall energy. All energy densities are scaled with $E_K^0 = \frac{1}{2}\rho\Omega^2 b^2$. The horizontal axis is Λ^{-1} , the inverse of the Elsasser number. It measures the ratio of the inertial force to the Lorentz force. The magnetic energy remains much smaller than the kinetic energy, but clearly increases with Λ^{-1} in both the experiments and the simulations: velocity fluctuations penetrate deeper into the fluid and induce larger magnetic fluctuations because the imposed magnetic field is stronger there.

4.4. The role of the Lorentz force

Although magnetic energies are much smaller than kinetic energies, the Lorentz force plays a major role. The strong imposed dipolar magnetic field governs the dynamics of the mean flow in the *DTS* experiment. In particular, the very efficient entrainment of the fluid by the conductive inner sphere, and the zone of super-rotation next to it, are entirely due to the presence of the magnetic field.

In order to see the effect of the Lorentz force on the fluctuations, we have run a

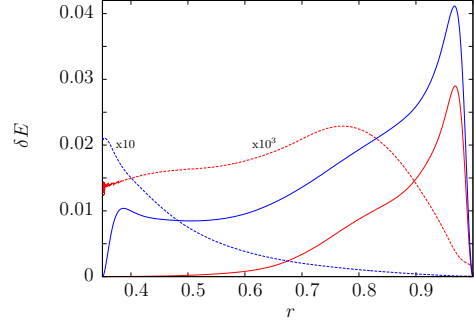


FIGURE 14. Time-and-angles-averaged energy of fluctuations as a function of radius r . This plot compares the kinetic (solid lines) and magnetic (dashed lines) energies of the reference simulation (in red) with a simulation (in blue) with the same parameters ($Pm = 10^{-3}$, $Re = 2611$ and $\Lambda = 3.4 \times 10^{-2}$), but in which the Lorentz force has been nulled out for $m \neq 0$. Note that the magnetic energy is two orders of magnitude larger in the latter case.

simulation in which the Lorentz force is nulled out except for $m = 0$. We find that the radial profile of angular velocity at the equator remains essentially the same, illustrating that non-linear interactions of fluctuations with $m \neq 0$ barely contribute to the mean flow. Frequency spectra of the surface magnetic field (figure 13a) still display spectral bumps, but they are narrower and much more intense. Furthermore, the azimuthal mode number analysis (figure 13b) reveals that modes of a given m show up at several distinct frequencies.

The damping effect of the Lorentz force is best illustrated by plots of the radial profile of the energy of the fluctuations. Figure 14 displays the resulting radial profiles of the kinetic and magnetic energies, integrated over time and colatitude. While the kinetic energy of the fluctuations is negligible for $r < 0.6$ when the Lorentz force is present, fluctuations invade the complete fluid shell when it is suppressed. Fluctuations are largest beneath the outer shell where the magnetic field is weakest, but even there fluctuations are much weaker when the Lorentz force is active.

The magnetic energy of the fluctuations reaches only a thousandth of the kinetic energy in the *DTs* configuration. Not surprisingly, when the Lorentz force is suppressed, it jumps by a factor of 100 near the inner sphere, where the imposed magnetic field is strongest. This demonstrates how dangerous it can be to infer magnetic energy and dissipation from flow solutions computed without the feedback of the Lorentz force (see discussion between Glatzmaier (2008) and Liu *et al.* (2008)).

5. Discussion

We have obtained bumpy frequency spectra in numerical simulations of the magnetized spherical Couette flow. They compare very well with spectra obtained in the *DTs* experiment from magnetic and electric time-records (Schmitt *et al.* 2008). As in the experiment, the dominant azimuthal mode number is incremented by 1 from one frequency bump to the next. Very large Reynolds numbers are not required for getting this behaviour, but one needs to accumulate long time-series (typically 300 turns of the inner sphere) for the peaks to show up clearly in the spectra.

We have developed a new method, which bridges the gap between the linear modal approach (Rieutord & Valdettaro 1997; Kelley *et al.* 2007; Schmitt *et al.* 2008) and full non-linear simulations and experiments. By performing a time-domain Fourier transform

of the full fields for each azimuthal number m , we recover the dominant frequencies and obtain the structure of the modes, which can then be compared to linear solutions and to experimental observations. We think that this approach will help identifying the mode selection mechanism in other experiments (Kelley *et al.* 2010).

Snap-shots and spatio-temporal plots reveal a rather different story, in which chaotic instabilities are swept by the flow. We could show that these two views are dual: since the instabilities circle around the sphere, the parts that are in phase between two successive passages are statistically enhanced.

The maps of the kinetic and magnetic energies of the fluctuations indicate that they initiate in the outer boundary layer, which is of the Bödewadt type, with only minor influence of the magnetic field. The parallel-flow absolute instability analysis of Lingwood (1997) yields a good prediction of the azimuthal mode number of the instabilities and of the Reynolds number at which they appear. The fluctuations of kinetic energy are much larger than that of magnetic energy, which are mostly slave of the former. Both the *DTS* measurements and our numerical simulations display a strong increase of the magnetic energy fluctuations when getting closer to the inner sphere. This appears to be essentially the consequence of the strong increase of the imposed dipolar field there.

At first order, we expect both energies to be proportional to the square of the imposed inner sphere velocity. However, we note that when this effect is taken into account, the scaled kinetic energy tends to decrease when the forcing is increased, while the scaled magnetic energy increases. Brito *et al.* (2011) showed that the energy of the mean flow behaves similarly, and proposed that this is a consequence of the increasing turbulent friction at the outer surface: as the friction increases, the core-flow is slowed down, while the shear between the spinning inner sphere and the fluid increases, inducing a stronger magnetic field. We think that another effect explains the trend observed for the energy fluctuations: as the forcing increases, the damping effect of the magnetic field decreases. Instabilities penetrate deeper into the fluid and produce larger magnetic fluctuations, even though their scaled kinetic energy is reduced because of the decreased velocity drop across the outer boundary layer.

Although the magnetic energy is very small, the Lorentz force plays a major role: it determines the very efficient entrainment of the fluid by the spinning inner sphere, but it also heavily damps the fluctuations in most of the fluid. When we remove the Lorentz force for $m \neq 0$, fluctuations invade the fluid, and sharper and more numerous frequency peaks are observed in the spectra. This gets closer to the observations of Kelley *et al.* (2007), where the imposed magnetic field was weak and only served as a marker of the flow. It could also explain the sharp ‘ N ’ modes reported by Schmitt *et al.* (2008) for the largest rotation rates in the *DTS* experiment.

One could have expected instabilities to develop in the inner region near the equator, where the flow obeys Ferraro law. This does not appear to be the case. In the present study, we have kept the Lundquist number small, as in the *DTS* experiment. Alfvén waves are therefore damped out rapidly. They might still contribute to shaping the modes near the inner sphere. It would be interesting to investigate the turbulent regime in the *DTS* geometry at larger Lundquist number.

Our study emphasizes the role of boundary layer instabilities in feeding turbulence inside the fluid. In the Earth’s core, large-scale flow velocities are in the mm/s-range. For these values, the Ekman-Hartmann layer at the top of the core appears to be mildly unstable (Desjardins *et al.* 2001). While turbulence in the Earth’s core has mainly been viewed as being produced by thermal plumes (Braginsky & Meytlis 1990), we suggest that instabilities at the core-mantle boundary could play a role as well.

We thank D. Jault for stimulating discussions. We gratefully acknowledge the support of CNRS and Université de Grenoble through the collaborative program “Turbulence, Magnetohydrodynamics and Dynamo”.

Supplementary movies are available at journals.cambridge.org/flm.

Movie 1. Map view of the time evolution of the azimuthal velocity beneath the surface of the outer sphere ($r = 0.95$) in the reference numerical simulation ($Pm = 10^{-3}$, $Re = 2611$ and $\Lambda = 3.4 \times 10^{-2}$). At the origin time, the fluid is at rest and the rotation rate of the inner sphere is set to f . The frame index is displayed. There are 6 frames per turn. The movie lasts 100 turns. Note that the first instabilities appear at the equator and are axisymmetric. After about 24 turns, non-axisymmetric instabilities show up.

Movie 2. Time evolution of the angular velocity in a meridional plane ($\varphi = 0$) for the same simulation as in movie 1.

REFERENCES

- BALBUS, S.A. & HAWLEY, J.F. 1991 A powerful local shear instability in weakly magnetized disks. 1. linear analysis. *Astrophysical Journal* **376** (1, Part 1), 214–222.
- BERHANU, M., MONCHAUX, R., FAUVE, S., MORDANT, N., PÉTRÉLIS, F., CHIFFAUDEL, A., DAVIAUD, F., DUBRULLE, B., MARIÉ, L., RAVELET, F., BOURGOIN, M., ODIER, P., PINTON, J.-F. & VOLK, R. 2007 Magnetic field reversals in an experimental turbulent dynamo. *Europhys. Lett.* **77**, 59001–+.
- BÖDEWADT, U.T. 1940 Die Drehstromung über festem Grund. *Z. Angew. Math. Mech.* **20**, 241–253.
- BRAGINSKY, SI & MEYTLIS, VP 1990 Local turbulence in the earth’s core. *Geophysical & Astrophysical Fluid Dynamics* **55** (2), 71–87.
- BRITO, D., ALBOUSSIÈRE, T., CARDIN, P., GAGNIÈRE, N., JAULT, D., LA RIZZA, P., MASSON, J. P., NATAF, H. C. & SCHMITT, D. 2011 Zonal shear and super-rotation in a magnetized spherical Couette-flow experiment. *Physical Review E* **83** (6, Part 2).
- BUSSE, F. H. 1970 Thermal instabilities in rapidly rotating systems. *J. Fluid Mech.* **44**, 441–460.
- CARDIN, P., BRITO, D., JAULT, D., NATAF, H.-C. & MASSON, J-P 2002 Towards a rapidly rotating liquid sodium dynamo experiment. *Magnetohydrodynamics* **38**, 177–189.
- DESJARDINS, B., DORMY, E. & GRENIER, E. 2001 Instability of ekman–hartmann boundary layers, with application to the fluid flow near the core–mantle boundary. *Physics of the Earth and Planetary Interiors* **123** (1), 15–26.
- DORMY, E., CARDIN, P. & JAULT, D. 1998 MHD flow in a slightly differentially rotating spherical shell, with conducting inner core, in a dipolar magnetic field. *Earth Planet. Sci. Lett.* **160**, 15–30.
- ELSASSER, W. M. 1946 Induction Effects in Terrestrial Magnetism Part I. Theory. *Phys. Rev.* **69** (3-4), 106–116.
- FERRARO, V.C.A. 1937 The non-uniform rotation of the sun and its magnetic field. *Mon. Not. Roy. Astron. Soc.* **97**, 458.
- FRICK, P., NOSKOV, V., DENISOV, S. & STEPANOV, R. 2010 Direct Measurement of Effective Magnetic Diffusivity in Turbulent Flow of Liquid Sodium. *Physical Review Letters* **105** (18).
- GAILITIS, A., LIELAUSIS, O., PLATACIS, E., DEMENT’EV, S., CIFERSONS, A., GERBETH, G., GUNDRUM, T., STEFANI, F., CHRISTEN, M. & WILL, G. 2001 Magnetic Field Saturation in the Riga Dynamo Experiment. *Phys. Rev. Lett.* **86**, 3024–3027.
- GAUTHIER, G., GONDRET, P. & RABAUD, M. 1999 Axisymmetric propagating vortices in the flow between a stationary and a rotating disk enclosed by a cylinder. *Journal of Fluid Mechanics* **386**, 105–126.
- GISSINGER, C., JI, H. & GOODMAN, J. 2011 Instabilities in magnetized spherical Couette flow. *Physical Review E* **84** (2, Part 2).
- GLATZMAIER, G. A. 2008 A note on “Constraints on deep-seated zonal winds inside Jupiter and Saturn”. *Icarus* **196**, 665–666.

- GLATZMAIER, G. A. & ROBERTS, P. H. 1995 A three-dimensional self-consistent computer simulation of a geomagnetic field reversal. *Nature* **377**, 203–+.
- JAULT, D. 2008 Axial invariance of rapidly varying diffusionless motions in the Earth's core interior. *Phys. Earth Planet. Inter.* **166**, 67–76.
- KAPLAN, E. J., CLARK, M. M., NORNBERG, M. D., RAHBARNIA, K., RASMUS, A. M., TAYLOR, N. Z., FOREST, C. B. & SPENCE, E. J. 2011 Reducing Global Turbulent Resistivity by Eliminating Large Eddies in a Spherical Liquid-Sodium Experiment. *Physical Review E* **106** (25).
- KELLEY, D.H., TRIANA, S.A., ZIMMERMAN, D.S. & LATHROP, D.P. 2010 Selection of inertial modes in spherical Couette flow. *Physical Review E* **81** (2, Part 2).
- KELLEY, D.H., TRIANA, S.A., ZIMMERMAN, D.S., TILGNER, A. & LATHROP, D.P. 2007 Inertial waves driven by differential rotation in a planetary geometry. *Geophys. Astrophys. Fluid Dyn.* **101** (5-6), 469–487, 10th Symposium on the Study of the Earths Deep Interior (SEDI), Prague, Czech Republic, Jul 09-14, 2006.
- LARMOR, J. 1919 How could a Rotating Body such as the Sun become a Magnet? *Report of the British Association for the Advancement of Science 87th meeting*, 159–160.
- LATHROP, D.P. & FOREST, C.B. 2011 Magnetic dynamos in the lab. *Physics Today* **64** (7), 40–45.
- LE BARS, M., WIECZOREK, M. A., KARATEKIN, O., CEBRON, D. & LANEUVILLE, M. 2011 An impact-driven dynamo for the early Moon. *Nature* **479**, 215–218.
- LINGWOOD, R.J. 1997 Absolute instability of the Ekman layer and related rotating flows. *Journal of Fluid Mechanics* **331**, 405–428.
- LIU, J., GOLDBREICH, P. M. & STEVENSON, D. J. 2008 Constraints on deep-seated zonal winds inside Jupiter and Saturn. *Icarus* **196**, 653–664.
- LOPEZ, J.M., MARQUES, F., RUBIO, A.M. & AVILA, M. 2009 Crossflow instability of finite Bödewadt flows: Transients and spiral waves. *Physics of Fluids* **21** (11), 114107.
- MATSUI, H., ADAMS, M., KELLEY, D., TRIANA, S. A., ZIMMERMAN, D., BUFFETT, B. A. & LATHROP, D. P. 2011 Numerical and experimental investigation of shear-driven inertial oscillations in an Earth-like geometry. *Physics of the Earth and Planetary Interiors* **188**, 194–202.
- MONCHAUX, R., BERHANU, M., BOURGOIN, M., MOULIN, M., ODIER, P., PINTON, J.-F., VOLK, R., FAUVE, S., MORDANT, N., PÉTRÉLIS, F., CHIFFAUDEL, A., DAVIAUD, F., DUBRULLE, B., GASQUET, C., MARIÉ, L. & RAVELET, F. 2007 Generation of a Magnetic Field by Dynamo Action in a Turbulent Flow of Liquid Sodium. *Phys. Rev. Lett.* **98** (4), 044502–+.
- MORESCO, P. & ALBOUSSIÈRE, T. 2004 Stability of Bödewadt-Hartmann layers. *European Journal of Mechanics - B/Fluids* **23** (6), 851–859.
- NATAF, H.-C., ALBOUSSIÈRE, T., BRITO, D., CARDIN, P., GAGNIÈRE, N., JAULT, D., MASSON, J.-P. & SCHMITT, D. 2006 Experimental study of super-rotation in a magnetostrophic spherical Couette flow. *Geophys. Astrophys. Fluid Dyn.* **100**, 281–298.
- NATAF, H.-C., ALBOUSSIÈRE, T., BRITO, D., CARDIN, P., GAGNIÈRE, N., JAULT, D. & SCHMITT, D. 2008 Rapidly rotating spherical Couette flow in adipolar magnetic field: an experimental study of the mean axisymmetric flow. *Phys. Earth Planet. Inter.* **170**, 60–72.
- NOIR, J., HEMMERLIN, F., WICHT, J., BACA, S.M. & AURNOU, J.M. 2009 An experimental and numerical study of librational driven flow in planetary cores and subsurface oceans. *Physics of the Earth and Planetary Interiors* **173** (1-2), 141 – 152.
- NORNBERG, M. D., JI, H., SCHARTMAN, E., ROACH, A. & GOODMAN, J. 2010 Observation of Magnetocoriolis Waves in a Liquid Metal Taylor-Couette Experiment. *Phys. Rev. Lett.* **104** (7).
- RIEUTORD, M. & VALDETTARO, L. 1997 Inertial waves in a rotating spherical shell. *Journal of Fluid Mechanics* **341**, 77–99.
- SAVAS, Ö.M. 1987 Stability of Bödewadt flow. *Journal of Fluid Mechanics* **183** (1), 77–94.
- SCHAEFFER, N. 2012 Efficient Spherical Harmonic Transforms aimed at pseudo-spectral numerical simulations. *ArXiv e-prints* .
- SCHMITT, D., ALBOUSSIÈRE, T., BRITO, D., CARDIN, P., GAGNIÈRE, N., JAULT, D. & NATAF, H.-C. 2008 Rotating spherical Couette flow in a dipolar magnetic field : Experimental study of magneto-inertial waves. *J. Fluid Mech.* **604**, 175–197.

- SCHMITT, D., CARDIN, P., JAULT, D., LA RIZZA, P. & NATAF, H.-C. 2012 Magneto-Coriolis waves in a spherical Couette flow experiment. *submitted* .
- SCHOUVEILER, L., LE GAL, P. & CHAUVE, MP 2001 Instabilities of the flow between a rotating and a stationary disk. *Journal of Fluid Mechanics* **443**, 329–350.
- SISAN, D. R., MUJICA, N., TILLOTSON, W. A., HUANG, Y.-M., DORLAND, W., HASSAM, A. B., ANTONSEN, T. M. & LATHROP, D. P. 2004 Experimental Observation and Characterization of the Magnetorotational Instability. *Phys. Rev. Lett.* **93** (11), 114502–+.
- STIEGLITZ, R. & MÜLLER, U. 2001 Experimental demonstration of a homogeneous two-scale dynamo. *Phys. Fluids* **13**, 561–564.